

Imbalance in the response of pre- and post-synaptic components to amyloidopathy

Article

Published Version

Creative Commons: Attribution 4.0 (CC-BY)

Open Access

Stephen, T.-L., Tamagnini, F. ORCID: <https://orcid.org/0000-0002-8741-5094>, Piegsa, J., Sung, K., Harvey, J., Oliver-Evans, A., Murray, T. K., Ahmed, Z., Hutton, M. L., Randall, A., O' Neill, M. J. and Jackson, J. S. (2019) Imbalance in the response of pre- and post-synaptic components to amyloidopathy. *Scientific Reports*, 9. 14837. ISSN 2045-2322 doi: <https://doi.org/10.1038/s41598-019-50781-1> Available at <https://centaur.reading.ac.uk/87034/>

It is advisable to refer to the publisher's version if you intend to cite from the work. See [Guidance on citing](#).

To link to this article DOI: <http://dx.doi.org/10.1038/s41598-019-50781-1>

Publisher: Nature Publishing Group

All outputs in CentAUR are protected by Intellectual Property Rights law, including copyright law. Copyright and IPR is retained by the creators or other copyright holders. Terms and conditions for use of this material are defined in the [End User Agreement](#).

www.reading.ac.uk/centaur

CentAUR

Central Archive at the University of Reading

Reading's research outputs online

OPEN

Imbalance in the response of pre- and post-synaptic components to amyloidopathy

Received: 10 May 2019

Accepted: 12 September 2019

Published online: 16 October 2019

Terri-Leigh Stephen^{1,4}, Francesco Tamagnini^{1,2,3}, Judith Piegsa^{1,3}, Katherine Sung¹, Joshua Harvey¹, Alice Oliver-Evans¹, Tracey K. Murray¹, Zeshan Ahmed¹, Michael L. Hutton¹, Andrew Randall³, Michael J. O'Neill^{1,5} & Johanna S. Jackson^{1,6} 

Alzheimer's disease (AD)-associated synaptic dysfunction drives the progression of pathology from its earliest stages. Amyloid β ($A\beta$) species, both soluble and in plaque deposits, have been causally related to the progressive, structural and functional impairments observed in AD. It is, however, still unclear how $A\beta$ plaques develop over time and how they progressively affect local synapse density and turnover. Here we observed, in a mouse model of AD, that $A\beta$ plaques grow faster in the earlier stages of the disease and if their initial area is $> 500 \mu\text{m}^2$; this may be due to deposition occurring in the outer regions of the plaque, the plaque cloud. In addition, synaptic turnover is higher in the presence of amyloid pathology and this is paralleled by a reduction in pre- but not post-synaptic densities. Plaque proximity does not appear to have an impact on synaptic dynamics. These observations indicate an imbalance in the response of the pre- and post-synaptic terminals and that therapeutics, alongside targeting the underlying pathology, need to address changes in synapse dynamics.

Alzheimer's disease (AD) is the world's leading cause of dementia and is thought to be primarily a synaptopathy^{1,2}. Indeed, synapse loss and altered connectivity occurs in the earliest stages of AD, preceding its histopathological hallmarks and possibly driving the progression of cognitive decline^{3–6}. Mutations in the gene encoding the amyloid precursor protein (APP) carry the greatest incidence of early-onset familial AD (FAD), along with presenilin 1 and 2⁷. APP is widely expressed in neurons and is thought to be responsible for synapse formation and repair⁸. Animal models with human APP mutations exhibit synapse loss⁹ and dysfunction¹⁰, gliosis¹¹, cognitive impairments¹² and, in some cases, neuron loss¹⁰ alongside the progressive accumulation of pathogenic $A\beta$ species¹³.

To further understand synapse dynamics in amyloidopathy, we used the J20 mouse model, which has human APP mutations consistent with FAD^{14,15}. In this model, soluble $A\beta$ is apparent at 2 months of age, with the first plaques forming in the 5th month, in some animals, and in all animals by the 10th month¹⁶. From the moment $A\beta$ plaques start to appear, pathogenic amyloid species are not uniformly distributed across the brain parenchyma. Consequently, there may be differing effects on synapse structure and function in relation to their proximity to plaques⁹. Previous observations identified an inverse relationship between dendritic spine density and amyloid plaque pathology^{9,17}.

As $A\beta$ deposits represent a reservoir of pathogenic amyloid species, we first investigated plaque growth rates in relation to their initial area, plaque region and animal's age *in vivo*, using the amyloid-binding dye methoxy-XO4¹⁸, which labels both condensed cores and the surrounding fibrillar $A\beta$ subspecies¹⁹, referred to here as the cloud. In addition, we hypothesized that synapse density and turnover in the neocortex are altered in the presence of $A\beta$ plaques between 7 and 10 months of age and are differentially affected by plaque proximity.

¹Eli Lilly and Company, Lilly Research Centre, Erl Wood Manor, Windlesham, Surrey, GU20 6PH, UK. ²School of Pharmacy, University of Reading, Whiteknights Campus, Hopkins Building, Reading, RG6 6LA, UK. ³Institute of Biomedical and Clinical Sciences, University of Exeter Medical School, Hatherly Laboratories, University of Exeter, Exeter, EX4 4PS, UK. ⁴Present address: Department of Gerontology, University of Southern California, Los Angeles, California, 90089, USA. ⁵Present address: AbbVie Deutschland GmbH & Co. K.G., Ludwigshafen, Germany. ⁶Present address: UK Dementia Research Institute at Imperial College, Department of Brain Sciences, Imperial College London, London, UK. Terri-Leigh Stephen and Francesco Tamagnini contributed equally. Correspondence and requests for materials should be addressed to J.S.J. (email: johanna.jackson@imperial.ac.uk)

Results

To measure synapse dynamics in relation to plaque deposition in AD-associated amyloidopathy, we used *in vivo* two-photon imaging of methoxy-XO4-labelled plaques and GFP-expressing pyramidal neurons in the somatosensory cortex (SSC) of J20 mice and wild-type (WT) littermate controls (Fig. 1a). The same regions of interest were imaged longitudinally on a weekly basis. We studied two groups of J20 animals at different ages ranging from early (30–42 weeks/7–10 months old) to late stages (49–61 weeks/11–14 months old) (Fig. 1b) of the disease. WT littermates were used as a negative control cohort for the younger age-point (30–42 weeks/old) only. Both of the stages evaluated were characterized by the presence of pathogenic A β species and synapse loss in transgenic animals^{16,20}.

Amyloid plaque growth-rate is faster in younger animals and for larger plaques. The total area of A β plaques increased in both the early and late cohorts (Fig. 1c and S.Fig. 1, early $p = 0.0002$ and 1b late $p = 0.0002$). The plaque-to-plaque average growth rate (Rate of Rise; RoR, units: $\mu\text{m}^2/\text{week}$) was measured as the slope of a linear function fit for each plaque's surface area over time. We observed that A β plaques grew faster in younger animals (Fig. 1c right, $p < 0.0001$). As the plaques were not homogenous in size, we separated them into three groups, based on the initial raw total area: small ($< 300 \mu\text{m}^2$) medium ($300\text{--}500 \mu\text{m}^2$) and large ($> 500 \mu\text{m}^2$). Plaques that are initially large and those found in younger animals grew faster (Fig. 1d, $p = 0.001$ and $p < 0.0001$, respectively); in addition, age and plaque initial size interact in affecting plaque growth rate (Fig. 1d, $p = 0.0016$). For the complete set of pairwise comparisons, see SI-Table 1.

We separately investigated the growth rate of the plaque's dense core and surrounding cloud, across the two age-points (Fig. 1e). We observed that the age-point and the plaque region both affected and interacted with each other in relation to plaque growth rate (See insert in Fig. 1e for F and P values): the cloud grew faster than the core at both the early ($p < 0.0001$) and late (Bonferroni's corrected unpaired t-test; $p = 0.008$) groups. While, the core's growth rate was not different (Bonferroni's corrected unpaired t-test; $p = 0.542$), the cloud's growth rate was faster in the early group, compared to the late group ($p < 0.0001$). For the complete set of pairwise comparisons, see SI-Table 2. From these results, we can conclude that plaques grow faster in younger animals and if they have a large cloud surrounding the core. This is presumably due to A β aggregation occurring quicker at the level of the plaque cloud.

Axonal terminaux boutons but not dendritic spines are reduced in J20 transgenic mice. Hippocampal synapse loss has been observed in the J20 model as early as 3 months²⁰. However, the subtle differences between pre- and post-synaptic components have not been elucidated in relation to significant levels of amyloid, or in the cortex. Therefore, we examined whether the pre- and post-synaptic components (axonal terminaux boutons (TBs) and dendritic spines, respectively) of cytosolic GFP-transduced cortical pyramidal neurons, were altered in the J20 model, in an age range exhibiting significant plaque accumulation (between 7 and 10 months/30 and 42 weeks), compared to WT littermates (Fig. 2a). There was no overall observable difference in spine density (Fig. 2b, $p = 1$), however, there was a significant decrease in the density of TBs in J20s compared to WT controls in the SSC (Fig. 2c, $p = 0.04$).

The stability of dendritic spines and axonal boutons is altered in J20 transgenic mice. Continual addition and loss of synapses is thought to underlie the fine tuning of neuronal function to match cognitive demands^{21–24}. Disruption of synapse turnover or stability is thought to occur in disease, potentially indicative of the early stages of dementia^{25–27}. Thus, to further examine how synapse dynamics are altered in our model of amyloidopathy, spine and TB survival, as a fraction of the first-time point, were initially analyzed. There was a significant decrease in the survival fraction of both spines and TBs compared to WT control animals (Fig. 3a, spines $p = 0.04$ and TBs $p < 0.001$). The turnover ratio (TOR) was also disrupted, as there was a significant increase in the TOR for both dendritic spines and TBs in the J20 group (Fig. 3c, spines $p = 0.04$ and TBs $p < 0.001$). In addition, comparing the turnover of spines and TBs, as an average of all the time points, indicated a significantly higher turnover of TBs compared to spines in J20s (Fig. 3e, $p = 0.01$). On further analysis, this disruption in turnover was driven by an increase in gained spines while the number of lost spines was unaffected (Fig. 3f, gains $p = 0.02$ losses $p = 0.06$). The increased turnover of axonal TBs was driven by both gained and lost boutons (Fig. 3g, gains $p = 0.02$ losses $p = 0.004$). These observations reveal that, in the J20 model, both spines and TBs are less stable and the balance of turnover is significantly disrupted at the level of both the pre- and post-synapse.

Alterations in synapse density and stability is not affected by plaque proximity. As previously shown, synapse density is negatively correlated to the proximity of amyloid plaques in the Tg2576 (APP Swedish mutation) A β overexpressing transgenic mouse²⁸. Thus, we aimed to assess this in the J20 amyloid model. The proximity of the nearest plaque was measured for each axon or dendrite (Fig. 4a). Neurites were considered close to a plaque if the nearest plaque was within 300 μm . The densities of both axonal and dendritic synapse components were not differentially affected if the nearest plaque was less than 300 μm away when compared to those without a plaque nearby at any time point (Fig. 4b, $p = 0.5$ and c, $p = 0.2$). Notably, new plaques appeared during our longitudinal imaging periods, meaning plaques were at different stages of maturity and of different sizes. Consequently, we decided to consider a neuronal process as close to a newly formed plaque at five weeks post-plaque appearance. However, newly formed plaque distance did not significantly correlate with the spine or TB density (Fig. 4e, $p = 0.7$ and $p = 0.2$, respectively). The stability (Fig. 4e, spine $p = 0.7$ and TB $p = 0.08$) and turnover (Fig. 4f, spine $p = 1$ and TB $p = 0.2$) of spines and TBs was also unaffected by their proximity to the nearest plaque. Post-mortem evaluation of synaptophysin and PSD-95 puncta close to plaques confirmed that, even within 50 μm of plaques (Fig. 4g), pre-synaptic terminals (Fig. 4h, $p < 0.001$) were lost compared to WTs whereas post-synaptic spines were unaffected (Fig. 4i, $p > 0.05$).

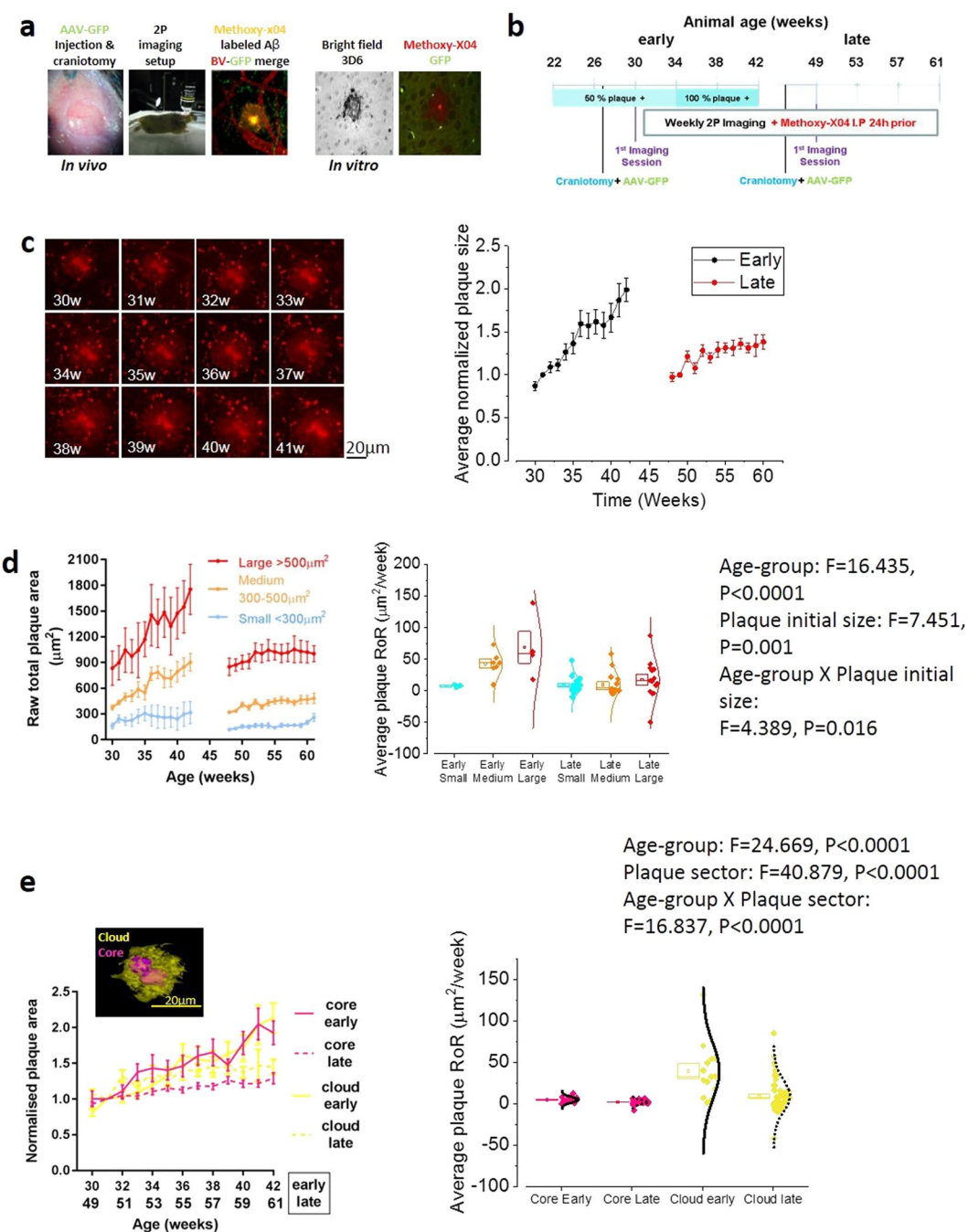


Figure 1. Amyloid plaque dynamics in AD-early vs late stage. **(a)** Imaging paradigm with example image of adeno-associated virus (AAV) GFP-transduced pyramidal neurons of the SSC (green) alongside blood vessels labelled with Texas-red (red) and plaques labelled with methoxy-X04 (yellow). Right images show colocalization of the A β antibody 3D6 and methoxy-X04 *ex vivo*. **(b)** Experimental timeline of early (30–42 weeks) and late (49–61 weeks) J20 groups. **(c)** Representative image series showing amyloid plaque growth starting at 30 weeks (left) and quantification of total plaque growth (right) normalized to the second imaging session (one-way analysis of variance (ANOVA), early p = 0.0002 and late p = 0.0002). Plaques grew faster in younger mice (unpaired t-test; p < 0.0001). **(d)** *Left:* raw total plaque area (μm^2) in the early and late groups separated into size categories; small (<200 μm^2 , blue), medium (200–500 μm^2 , orange) and large (>500 μm^2 , red). Small plaques (Two-way ANOVA, Factor: Plaque's initial size, Variable: slope, F = 7.451, p = 0.001) in younger animals (Two-way ANOVA, Factor: age, Variable: slope, F = 16.435, p < 0.0001) grew faster. *Right:* Scatter-box plot showing the plaque-to-plaque growth rate (Rate of Rise: RoR, units: $\mu\text{m}^2/\text{week}$) grouped per age and plaque's initial size. Two-way ANOVA revealed that both age and plaque initial size affect the plaque RoR (p = 0.02). Post-hoc Bonferroni corrected t-tests revealed that larger plaques grow faster in the early group (Two-way ANOVA, Factor: age \times Plaque's initial size, Variable: slope, F = 4.389, p = 0.0016 (SI Table 1)). In all scatter-box plot figures, the box represents the mean, the SEM boundaries (top and bottom line) and the median; the distribution line on the right shows the normality of the distribution for each data population.

(e) *Left:* Normalized area of the plaque cloud (yellow) and core (pink) in the early (broken lines) and late groups (solid lines). *Right:* plaque-to-plaque average RoR, grouped per age and plaque region. The cloud grew faster than the core (Bonferroni's corrected unpaired t-test; $p < 0.0001$) and only the clouds grew faster in younger mice (Bonferroni's corrected unpaired t-test; $p < 0.0001$). Early group $n = 13$ plaques, late group $n = 58$ plaques. Unless otherwise stated, data are presented as means \pm SEM.

Discussion

The loss of synapses in AD has been observed in humans and several mouse models^{2,29,30}, however, the specific, time-dependent dynamics of synaptic alterations warrants further investigation. Further, while the growth of amyloid plaques has been previously characterized *in vivo*^{30–34}, their growth dynamics, as a function of size and age, and the relationship between plaque growth and synapse dynamics still remains to be determined. Subtle changes in fine plaque and synaptic detail, and their interactions over time, captured here using *in vivo* multiphoton imaging, cannot readily be studied using conventional post-mortem analyses.

In this current study, we present three main findings: firstly, amyloid plaques grow at a faster rate if they are large and in young animals, secondly axonal boutons, but not dendritic spines, are lost in amyloidopathy and thirdly, the stability of both synaptic structures is compromised in the J20 transgenic model. The age- and size-dependent differences in plaque growth rate in J20 mice may be due to deposition dynamics occurring in the plaque cloud, rather than the dense core. This suggests that the main area of plaque growth may be the cloud: the slow growth of small plaques may be due to the reduced extension of the cloud. Age, plaque size and extension of the cloud, may be important for developing drug interventions³⁵.

Whilst we characterized the growth of individual plaques in this study, the overall density of plaques in the SSC also increased over this time period¹⁶. The growth of individual plaques was affected by the initial size, especially in the younger animals. The higher density of plaques in the older animals (late group) may account for the reduced growth with age³¹, contrary to what was seen by Hefendehl and colleagues in the APPPS1 model. This finding is largely consistent with Meyer-Luehmann and colleagues, who show that younger (and therefore smaller) plaques had an initial rapid increase in size before their growth rate slowed³². Another possibility is that larger plaques are formed by the clustering of small plaques³⁴. In this study, whilst we often saw plaques relatively close to each other (within a few hundred micrometers, although not as close as reported by McCarter and colleagues), we did not observe any plaques merging. There is a possibility that this had occurred before our imaging began, especially as we observed some larger plaques with two-lobed cores, so we cannot completely rule this out. Whilst it is possible that the different groups may have differing rates of A β production, the aggregated A β in both groups would be deposited either as a new plaque or join an existing plaque. In young animals, where more new plaques are developing³³, A β would join the relatively few existing plaques, reflected by a higher rate of growth in these plaques, especially in the plaque cloud. However, in older animals, where there are more plaques, new A β would be distributed amongst the many plaques present so each plaque would show a slower, possibly saturated, rate of growth. We hypothesize that the cloud consists of loosely packed fiber-like structures that extend outward from the densely packed core, as described previously¹⁹. Recent literature has proposed a link between plaque compaction and microglial-dependent plaque interactions that have a direct effect on the degree of neurite damage³⁶. Indeed, a study by Condello and colleagues has shown that rapidly growing plaques are associated with greater levels of local neuronal dystrophy and that this damage plateaus as plaque growth rate slows³⁷. Of further note, microglia have been shown to form a physical 'barrier' around plaques, limiting their expansion resulting in smaller, more compact plaques³⁸. This could explain the heterogeneity in plaque growth, where the growth rate of smaller plaques might be limited by microglia. It should be noted that the older group of animals received a control compound in a drug discovery study, which was not found to have an effect on amyloid pathology, although other more subtle effects cannot be ruled out. Finally, cerebral amyloid angiopathy (CAA) has been reported to occur in J20 mice^{39,40}. This is of relevance as the accumulation and growth of A β plaques is driven by both increased A β peptide production and decreased degradation and perivascular drainage, in both sporadic and FAD⁴¹. Teasing out the interplay of effects of A β toxic species on both vascular and neuronal function, will be of key importance in order to clarify the pathogenesis of AD. Although CAA was observed in these animals, we were careful to image plaques away from blood vessels to avoid it being a confounding factor in the parenchymal A β accumulation. To address the vascular effects of A β accumulation, we have recently investigated the function of the blood-brain barrier (BBB) in J20 mice and did not observe any differences between WTs and J20 animals (data not shown).

This is the first study of its kind to quantify the growth of different components of amyloid plaques (specifically comparing the cloud and the dense core), at different time points, using this temporal resolution. Overall, these observations help us to understand how amyloid pathology progresses over time and may help to identify patients for newly developed therapies. This could potentially be achieved by the validation of the detection of single A β plaques in the retina as a selective and specific diagnostic tool for AD⁴². A β plaque number, growth rate (both in number and size), cloud: core surface ratio and the correlation of these parameters with the cognitive state of the patient, may provide vital information on the progression of the disease and what therapeutic strategy may be the most effective, for individual patients.

To date, very few studies have looked at dendritic spine density in the J20 model. A 36% reduction was observed in the hippocampus at 11 months⁴³, however, equivalent measurements were not made in the cortex. Interestingly, Hong and colleagues reported a significant decrease in hippocampal PSD-95 puncta in J20 mice, at 3 months of age, without a change in synaptophysin staining in *ex vivo* sections²⁰. However, Mucke and colleagues¹⁶, who originally characterized the J20 model, reported a loss of synaptophysin terminals not correlated with plaque load, suggesting that plaques are not the cause of synapse loss, consistent with our findings. In the

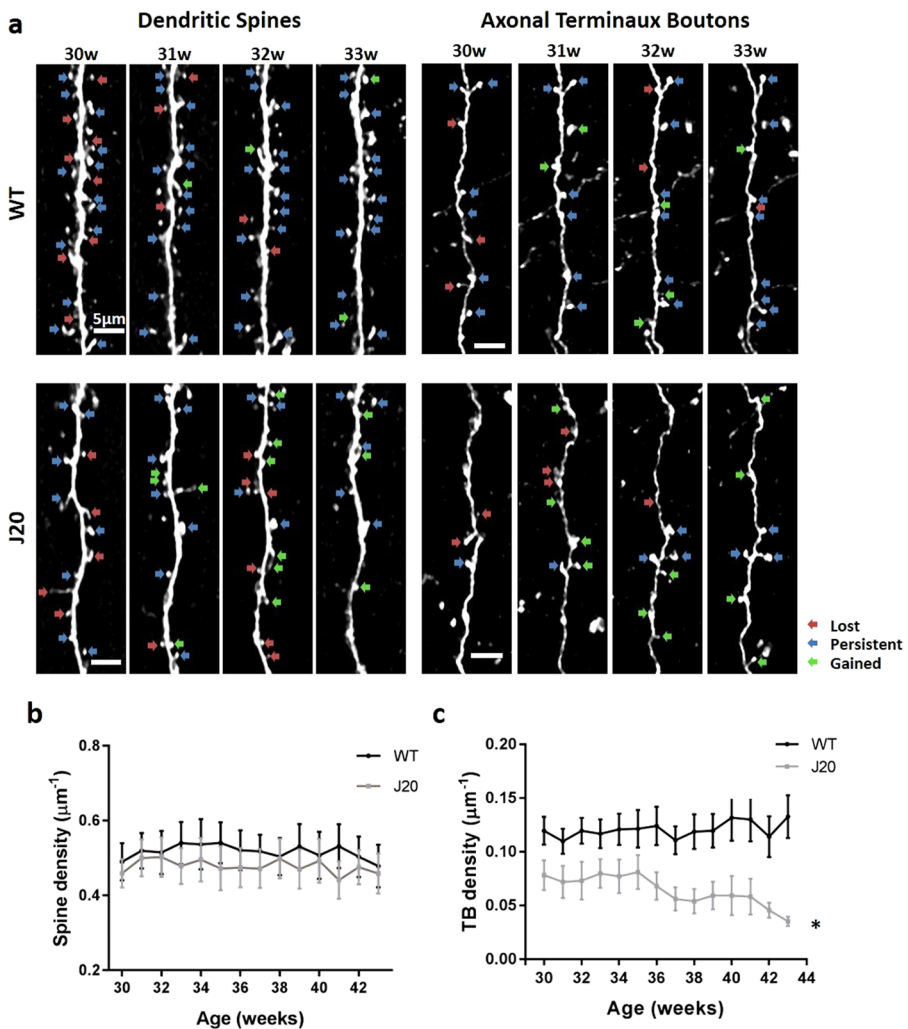


Figure 2. Axonal terminaux boutons but not dendritic spines are reduced in J20s. (a) Representative maximum projections of dendritic spines and axonal TBs in J20 animals and littermate controls (WT) at 30–33 weeks of age. Red arrows show lost, blue arrows show persistent and green arrows show gained spines/ boutons. (b) Quantification of dendritic spine density in J20s and WT control animals showing no significant difference (two-way repeated measure (RM) ANOVA genotype × age $F_{(605, 13)} = 0.32, p = 1$). (c) Quantification of TB density shows a progressive loss with age compared to WT controls (two-way RM ANOVA genotype × age $F_{(517, 13)} = 1.8, p = 0.04$). J20 spines n = 21, WT spines n = 34, J20 TBs n = 16, WT boutons n = 36. Error bars represent SEM.

Tg2576 model, Spires and colleagues reported a decrease in cortical spines⁹ and Bittner and colleagues showed a decrease in cortical and hippocampal spines in 3xTg mice (both within and >50 μm from plaques, but only from 13 months of age onwards)¹⁷. Here we show that dendritic spine density was unaffected in the cortex (both *in vivo* and by post-mortem analysis), possibly due to differences in AD models, brain region and/or plaque proximity. This finding was consistent with a previous study³⁰ reporting changes in spine density within 50 μm of plaques. However, we did observe a reduction in their survival and a change to their turnover, regardless of plaque proximity. The J20 model has not been reported to exhibit significant levels of neurodegeneration; in line with this we did not observe any dystrophic neurites. Other studies have shown dystrophic neurites and dramatic synapse loss around plaques, however, these occurred within 15 μm of a plaque⁴⁴. Here, neurites were imaged 50–200 μm from the nearest plaque edge, which would explain why no dystrophic neurites were observed. Therefore, axonal bouton loss was on cells that did not degenerate during the experimental time frame.

This study presents novel *in vivo* measurements of axonal bouton density, revealing a significant reduction in TBs. This is consistent with a loss of synaptophysin staining found here (Fig. 4h) and in other similar studies^{9,45}. However, Liebscher and colleagues did not show any change in bouton density either close to (<50 μm) or further from plaques (>50 μm) in male APPPS1 mice. Changes in turnover were only seen <50 μm from plaques³⁰. Liebscher and colleagues used a Thy-1 GFP-M model, which, they say, mainly labels cortical layer 5 cells. Their axonal morphology looks consistent with layer 5 labelling due to the high density of en passant boutons and fewer TBs⁴⁶. Using a virally targeted method, we observed staining in all cortical layers, however, most of the axonal labelling appeared to be from layer 6, due to the higher density of TBs, which are highly plastic⁴⁶. An explanation

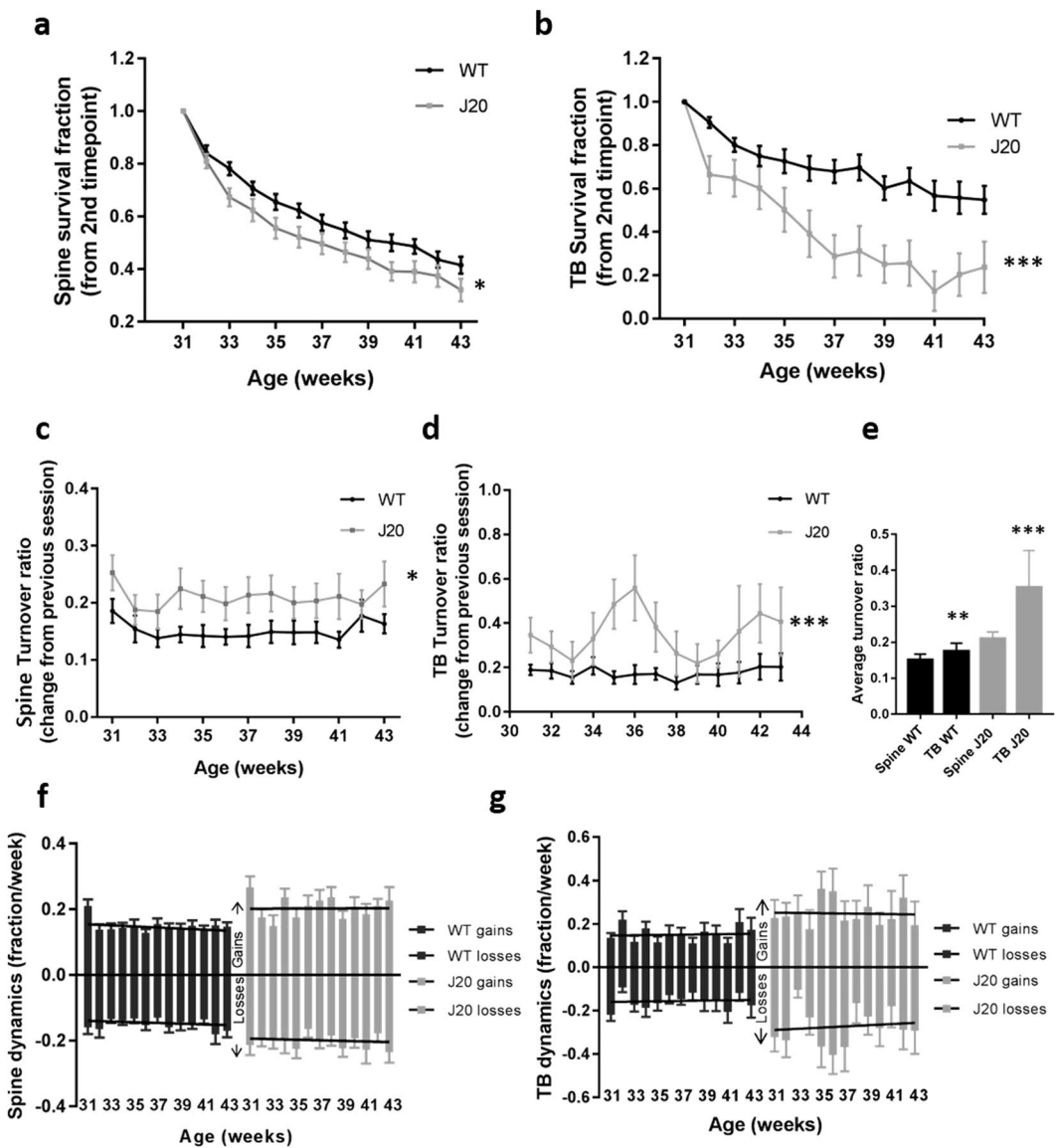


Figure 3. The stability of dendritic spines and axonal terminals is altered in J20s. **(a,b)** Quantification of spine (**a**; two-way RM ANOVA genotype $F_{(540,1)} = 4.4$, $p = 0.04$) and TB (**b**; two-way RM ANOVA genotype $F_{(461,1)} = 13.7$, $p < 0.001$) survival, as a fraction of the first time-point (30 weeks), in J20s and WT controls. **(c,d)** TOR, showing the change compared to the previous session, of spines (**c**; two-way RM ANOVA genotype $F_{(552,1)} = 4.4$, $p = 0.04$) and TBs (**d**; two-way RM ANOVA genotype $F_{(471,12)} = 112.3$, $p < 0.001$) in J20s and WT controls. **(e)** Average total turnover across all time points showed a significant difference in spine and TB TOR in the J20 group but not in the WTs (two-way ANOVA $F_{(103,1)} = 6.3$, $p = 0.01$). **(f,g)** Gains and losses of dendritic spines (**f**; two-way RM ANOVA gains genotype $F_{(552,1)} = 5.6$, $p = 0.02$; losses genotype $F_{(552,1)} = 3.8$, $p = 0.06$) and TBs (**g**; two-way RM ANOVA gains genotype $F_{(482,1)} = 5.8$, $p = 0.02$; losses genotype \times age $F_{(482,12)} = 2.5$, $p = 0.004$) in J20s compared to WT controls. J20 spines $n = 21$, WT spines $n = 34$, J20 TBs $n = 16$, WT TBs $n = 36$. Error bars represent SEM.

for the disparity in pre- and post-synaptic regulation could be that bouton loss occurs prior to spine loss in the cortex, where spines are subsequently upregulated to compensate for this, at least in the earlier stages of the disease. This ability may be lost in older animals and, thus, could explain the differences observed in the above-mentioned studies and our findings, with regards to spine density. Another explanation could be that axonal boutons are upregulated due to dendritic spine instability, but over compensation by the axons results in TB loss. Or, as a recent study has shown⁴⁷, A β is enriched only at the pre- and not at the post-synapse, which may also explain why, in our study, axonal boutons are more affected than dendritic spines. In addition, it is becoming clear that there are potential sex differences in these models, as seen in a recent report in the 5xFAD model of AD⁴⁸.

Further, the imbalance between the pre- and post-synaptic components, seen here, is consistent with what we have reported in the Tg4510 model of tauopathy²⁷. Whilst this mismatch may be explained in tauopathy by the movement of pathological tau to the somatodendritic compartment⁴⁹, the mechanisms of how A β causes synapse

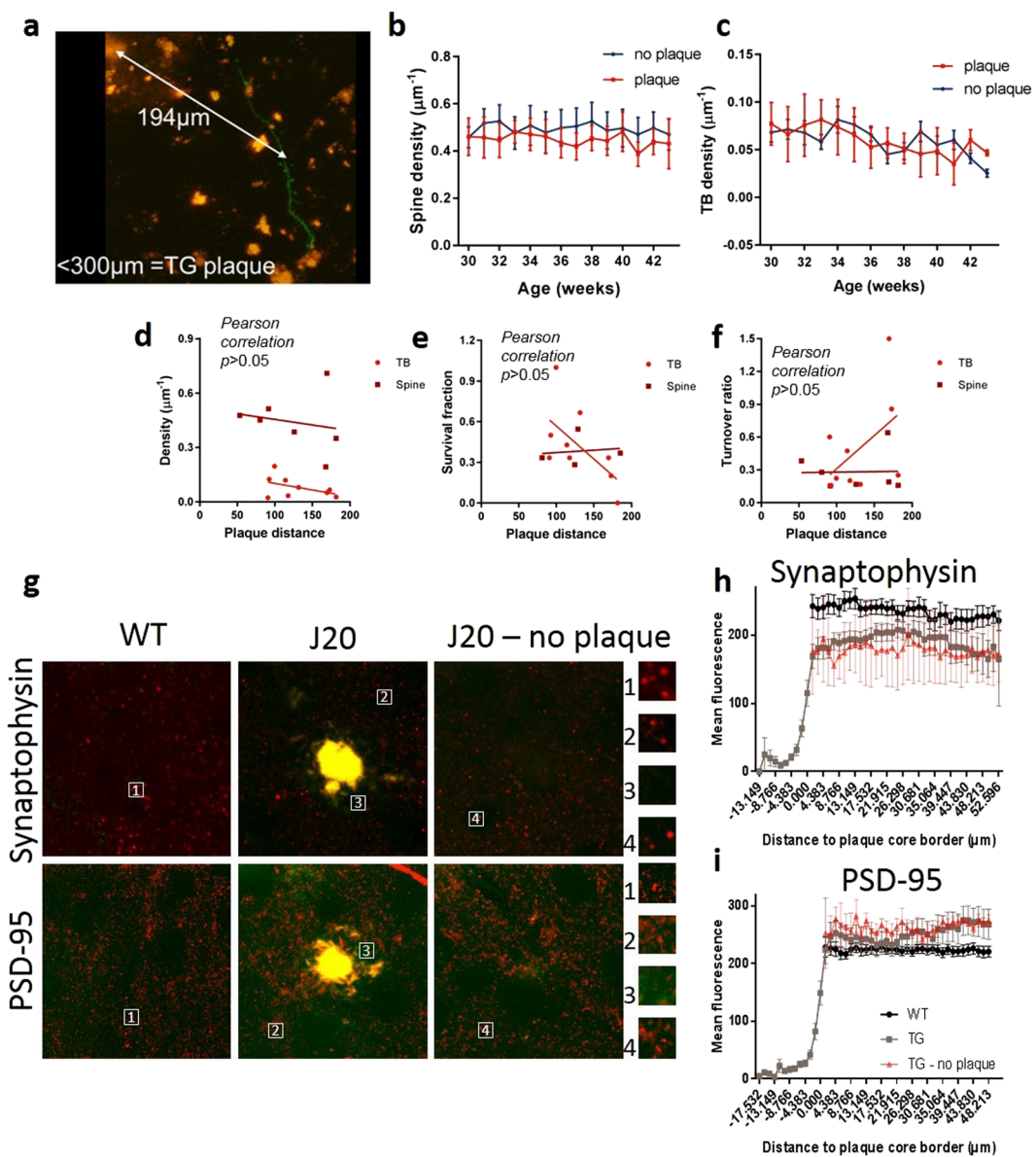


Figure 4. Changes in spine and bouton dynamics are not affected by plaque proximity or maturity. (a) The distance of each neurite to the center of the nearest plaque was measured. (b,c) Dendrites (b; two-way RM ANOVA plaque $F_{(204,1)} = 0.5$, $p = 0.5$) and axons (c; two-way RM ANOVA plaque $F_{(141,11)} = 1.7$, $p = 0.2$) within 300 μm of a plaque did not have a significant difference in synapse density compared to those further away from a plaque ($> 300 \mu\text{m}$). (d-f) Plaque distances were measured for each neurite five weeks post-plaque appearance, to control for the appearance of new plaques. This did not affect spine (d; Pearson correlation $p = 0.7$) or TB density (d; Pearson correlation $p = 0.2$), survival fraction (e; Pearson correlation, spines $p = 0.7$, TBs $p = 0.08$) or turnover ratio (f; Pearson correlation, spines $p = 1$, TBs $p = 0.2$). (g) CLARITY-cleared brain slices were stained for synaptophysin and PSD-95 and the immunoreactivity around plaques quantified. (h) Synaptophysin intensity was significantly reduced within 50 μm of plaques with a significant interaction between distance to plaque and group (two-way RM ANOVA $F_{(949,64)} = 2.5$, $p < 0.001$). (i) PSD-95 puncta intensity was not altered close to plaques (two-way RM ANOVA $F_{(1438,64)} = 0.5$, $p > 0.05$).

loss are less clear. Several studies have proposed candidate A β receptors such as p75NTR⁵⁰, Frizzled⁵¹ and LirB2/PirB⁵², all of which have been implicated in altered synaptic plasticity, but mainly on the post-synaptic side^{51–53}. Presumably, there is a soluble A β gradient, where synapses close to amyloid plaques are more likely to be lost through the toxic effects of soluble A β . Aside from this there could be a component of glial regulation implicated in this imbalance. Indeed, Hong and colleagues have shown that local activation of the innate immune system, via the glial complement system, mediates early synaptic loss in AD, before apparent plaque formation, and importantly, inhibiting this response ameliorates synapse loss²⁰. This highlights the importance of both astrocytes and microglia in AD-related synapse loss.

Another novel finding in this study was that, despite their stability, dendritic spine survival was significantly reduced. On the other hand, spine turnover, driven by the formation of newly formed spines, was increased, presumably leading to the maintenance of stable spine density. Conversely, the significant reduction in TB density was paralleled by the highly significant reduction in survival fraction and loss of TBs, with only a modest, but significant, increase in gained TBs, which was not sufficient to maintain a stable TB density. The loss of presynaptic boutons, but persistence of spine levels, would be sufficient to account for the decline in input-output relationships observed in multiple neurophysiological studies of synaptic transmission in murine models of amyloidopathy (reviewed in⁸), although other explanations are feasible, for example, changes in action potential waveforms⁵⁴.

In conclusion, our study reveals the unique, long-term growth dynamics of individual amyloid plaques and how this changes with disease progression. This is of particular importance when considering treatments that target amyloidopathy. In addition, our findings are consistent with previous work showing that synapses are targeted in amyloidopathy and we have shown, for the first time, that altered synapse dynamics leads to unstable synapses. Whilst studies are underway that seek to address the underlying pathology in AD and halt the disease, synaptic loss would still remain and continue to cause cognitive deficits. Thus, synaptic loss and instability would need to be addressed, alongside understanding the underlying mechanisms, for cognitive benefits in AD.

Materials and Methods

Animals. The J20 Aβ-overexpressing line carries a PDGF-β promoter-driven transgene for human APP, with *Indiana* (V717F) and *Swedish* (K670M – N671L) mutations. Both mutations are associated with FAD^{14,15}. Adult female mice of the J20 line ($n = 15$ animals) and WT littermate controls ($n = 15$ animals) were used from 7 months (27 weeks) of age. Adult female mice from 11 months (45 weeks) ($n = 14$ animals) were also used for plaque analysis. This second set of animals was administered with a control vehicle for a drug discovery study, however, it was confirmed, with post-mortem immunohistochemistry, that this had no effect on measures of amyloid pathology (data not shown). All mice were given *ad libitum* access to food and water and maintained in a 12-hour light-dark cycle. All procedures were conducted by researchers holding a UK personal license and experimental protocols were approved and conducted in accordance with the UK Animals (Scientific Procedures) Act 1986 and subject to internal ethical review (Animal Welfare and Ethical Review Board at Lilly UK).

Surgery. Cranial windows were surgically implanted over the SSC as previously described²⁷. Briefly, mice were anaesthetized with isofluorane and administered dexamethasone (30 mg/kg) to limit brain swelling and the analgesic, buprenorphine (5 mg/kg), pre-operatively. The skull was exposed and a 5 mm diameter craniotomy drilled over the SSC. AAV (serotype 2) expressing cytosolic enhanced-GFP was stereotactically injected into the SSC, ~300 μm below the dura. A glass coverslip was placed over the craniotomy and sealed with glue and dental cement. A screw was placed in the skull on the contralateral side for added stability. The whole skull was subsequently covered in dental cement and a metal bar placed on top to allow head fixation at the two-photon microscope. Mice were allowed to recover for 3 weeks before imaging began. It was confirmed, by immunohistochemistry, that the cranial window did not cause an increase in amyloid pathology or microgliosis in any of the groups (data not shown).

Imaging. 5 mg/kg methoxy-XO4 (45% PBS, 45% propylene glycol, 10% DMSO) (2.9 mM) was injected intraperitoneally 24 hours prior to two-photon imaging to label the fibrillary beta sheet deposits of amyloid plaques. 25 μl of dextran-Texas red was injected intravenously immediately prior to imaging to visualize blood vessels in some imaging sessions. A purpose built two-photon microscope equipped with a tunable coherent Ti:Sapphire laser (MaiTAI, SpectraPhysics) and PrairieView acquisition software was used for all imaging experiments. Mice were anaesthetized with isofluorane and secured to the microscope via the metal bar attached to the skull and a custom-built fixed support. Lacri-lube was applied to the eyes to prevent dehydration and temperature of >34°C maintained by a heating blanket and rectal thermal probe. An Olympus 10X objective (NA = 0.3) was used to identify characteristic blood vessels to reliably relocate regions-of-interest (ROIs) at each imaging time point. In each animal an Olympus 40× (NA = 0.8) water immersion objective was used to acquire several ROI stacks (300 μm × 300 μm, 512 × 512 pixels, z-step size = 3 μm for plaques or 75 μm × 75 μm, 512 × 512 pixels, z-step size = 0.5 μm for neurites). A pulsed 910 nm wavelength laser beam was used with a typical power at the sample of 35 mW.

Analysis. Two-photon images were converted into stacks with ImageJ and the StackReg plugin was used to align the GFP stacks in case of any movement. The GFP stacks were deconvolved with Huygens Deconvolution software using a quick maximum likelihood estimation with an experimentally-defined point-spread-function. The red channel stacks (with methoxy-XO4 signal) were left unprocessed. Plaque images were denoised and maximum projections created. Plaque area was measured by manually outlining the total plaque and subsequently the core and measuring the area in ImageJ. Only plaques >20 μm in diameter were analysed to avoid the possibility of noise/ debris being included. More specifically, the core was defined as the inner part of the plaque, characterized by a continuous perimeter and a higher, more compact fluorescence intensity. The cloud was defined as the area surrounding the core, characterized by a discontinuous (hazy) perimeter and a lower, less compact fluorescence intensity. Initial, pilot experiments found the core fluorescence intensity to be approximately double the cloud intensity and the cloud fluorescence intensity to be approximately three times higher than the background; although these parameters were not routinely measured in the final analyses. The cloud area was calculated by subtracting the core area from the total plaque area. Prior to this all images were blinded using a custom ImageJ plugin so that time points were unknown at the point of analysis. The average rate of rise (RoR; μm²/week) of each plaque, was measured as the slope of a linear function interpolated for the plaque-to-plaque surface value in time (weeks). For dendritic spine and axonal bouton analysis each time-point was registered to the second imaging

session using MIPAV and converted to a 4D stack using a custom ImageJ macro. Each neurite to be analyzed was traced and the length measured using another custom macro. Subsequently, the spines or boutons were manually counted using the cell counter ImageJ plugin. Spines/boutons were counted in 3D image stacks while maximum projections are shown in the figures. Only TBs, not en passant boutons, were counted and identified as protrusions emanating from side of the axon with a head and neck. From this the density (μm^{-1}) and TOR (survival, as a fraction of the first time-point) were calculated. Statistics were performed using GraphPad Prism 7 or Sigma Plot 13. RM ANOVA comparisons (with Holm-Sidak method post-test) were utilized where multiple comparisons were made, unless otherwise stated.

Research data. Due to confidentiality agreements with research collaborators, supporting data can only be made available to bona fide researchers subject to a non-disclosure agreement. Details of the data and how to request access are available on request to the corresponding author.

CLARITY staining. Transcardiac perfusion with 4% paraformaldehyde was performed in a separate cohort of J20 animals at 10 months of age. Brains were sliced in 1 mm sections (Brain matrix, Alto) after 1 to 5 days incubation in 4% paraformaldehyde. To preserve molecular information and structural integrity brain slices were incubated with a hydrogel solution (4% acrylamide and 0.25% VA-044 in 1X PBS). Therefore, the tubes were degassed and the hydrogel was allowed to polymerise for 3 h at 37 °C. The slices were transferred into clearing solution (SDS, sodium borate) at 37 °C using the X-CLARITY system (Logos Biosystems). The slices were placed in a tube containing 1 ml of 5% BSA. The required amount of primary antibody was pipetted directly in the BSA solution and incubated for 4 days at 37 °C. Excess of antibody was washed away with PBS for 3 × 2 h at 37 °C. Secondary antibodies diluted in 5% BSA were incubated for 4 days at 37 °C and excess removed by washing the slices with PBS for 3 × 2 h at 37 °C. Concentric circles 5 μm apart were drawn on maximum projection images around the plaque and the mean fluorescence measured radiating out from the edge of the plaque.

Data Availability

Due to confidentiality agreements with research collaborators, supporting data can only be made available to bona fide researchers subject to a non-disclosure agreement. Details of the data and how to request access are available on request to the corresponding author.

References

- Kerrigan, T. L. & Randall, A. D. A new player in the “synaptopathy” of Alzheimer’s disease - arc/arg 3.1. *Front Neurol* **4**, 9, <https://doi.org/10.3389/fneur.2013.00009> (2013).
- Selkoe, D. J. Deciphering the genesis and fate of amyloid beta-protein yields novel therapies for Alzheimer disease. *J Clin Invest* **110**, 1375–1381, <https://doi.org/10.1172/JCI16783> (2002).
- Canuet, L. *et al.* Network Disruption and Cerebrospinal Fluid Amyloid-Beta and Phospho-Tau Levels in Mild Cognitive Impairment. *J Neurosci* **35**, 10325–10330, <https://doi.org/10.1523/JNEUROSCI.0704-15.2015> (2015).
- Jackson, J. *et al.* Targeting the Synapse in Alzheimer’s Disease. *Front Neurosci* **13**, 735, <https://doi.org/10.3389/fnins.2019.00735> (2019).
- Scheff, S. W., Price, D. A., Schmitt, F. A. & Mufson, E. J. Hippocampal synaptic loss in early Alzheimer’s disease and mild cognitive impairment. *Neurobiol Aging* **27**, 1372–1384, <https://doi.org/10.1016/j.neurobiolaging.2005.09.012> (2006).
- Jack, C. R. Jr. *et al.* Hypothetical model of dynamic biomarkers of the Alzheimer’s pathological cascade. *Lancet Neurol* **9**, 119–128, [https://doi.org/10.1016/S1474-4422\(09\)70299-6](https://doi.org/10.1016/S1474-4422(09)70299-6) (2010).
- Lanoiselee, H. M. *et al.* APP, PSEN1, and PSEN2 mutations in early-onset Alzheimer disease: A genetic screening study of familial and sporadic cases. *PLoS Med* **14**, e1002270, <https://doi.org/10.1371/journal.pmed.1002270> (2017).
- Randall, A. D., Witton, J., Booth, C., Hynes-Allen, A. & Brown, J. T. The functional neurophysiology of the amyloid precursor protein (APP) processing pathway. *Neuropharmacology* **59**, 243–267, <https://doi.org/10.1016/j.neuropharm.2010.02.011> (2010).
- Spires, T. L. *et al.* Dendritic spine abnormalities in amyloid precursor protein transgenic mice demonstrated by gene transfer and intravital multiphoton microscopy. *J Neurosci* **25**, 7278–7287, <https://doi.org/10.1523/JNEUROSCI.1879-05.2005> (2005).
- Hsia, A. Y. *et al.* Plaque-independent disruption of neural circuits in Alzheimer’s disease mouse models. *Proc Natl Acad Sci USA* **96**, 3228–3233, <https://doi.org/10.1073/pnas.96.6.3228> (1999).
- Oakley, H. *et al.* Intraneuronal beta-amyloid aggregates, neurodegeneration, and neuron loss in transgenic mice with five familial Alzheimer’s disease mutations: potential factors in amyloid plaque formation. *J Neurosci* **26**, 10129–10140, <https://doi.org/10.1523/JNEUROSCI.1202-06.2006> (2006).
- Olesen, L. O. *et al.* Behavioural Phenotyping of APPswe/PS1deltaE9 Mice: Age-Related Changes and Effect of Long-Term Paroxetine Treatment. *PLoS One* **11**, e0165144, <https://doi.org/10.1371/journal.pone.0165144> (2016).
- Sasaguri, H. *et al.* APP mouse models for Alzheimer’s disease preclinical studies. *EMBO J* **36**, 2473–2487, <https://doi.org/10.15252/embj.201797397> (2017).
- Mullan, M. *et al.* A pathogenic mutation for probable Alzheimer’s disease in the APP gene at the N-terminus of beta-amyloid. *Nat Genet* **1**, 345–347, <https://doi.org/10.1038/ng0892-345> (1992).
- Murrell, J., Farlow, M., Ghetti, B. & Benson, M. D. A mutation in the amyloid precursor protein associated with hereditary Alzheimer’s disease. *Science* **254**, 97–99 (1991).
- Mucke, L. *et al.* High-level neuronal expression of abeta 1-42 in wild-type human amyloid protein precursor transgenic mice: synaptotoxicity without plaque formation. *J Neurosci* **20**, 4050–4058 (2000).
- Bittner, T. *et al.* Multiple events lead to dendritic spine loss in triple transgenic Alzheimer’s disease mice. *PLoS One* **5**, e15477, <https://doi.org/10.1371/journal.pone.0015477> (2010).
- Klunk, W. E. *et al.* Imaging Abeta plaques in living transgenic mice with multiphoton microscopy and methoxy-X04, a systemically administered Congo red derivative. *J Neuropathol Exp Neurol* **61**, 797–805 (2002).
- Wang, Y. *et al.* TREM2-mediated early microglial response limits diffusion and toxicity of amyloid plaques. *J Exp Med* **213**, 667–675, <https://doi.org/10.1084/jem.20151948> (2016).
- Hong, S. *et al.* Complement and microglia mediate early synapse loss in Alzheimer mouse models. *Science* **352**, 712–716, <https://doi.org/10.1126/science.aad8373> (2016).
- Trachtenberg, J. T. *et al.* Long-term *in vivo* imaging of experience-dependent synaptic plasticity in adult cortex. *Nature* **420**, 788–794, <https://doi.org/10.1038/nature01273> (2002).

22. Holtmaat, A., Wilbrecht, L., Knott, G. W., Welker, E. & Svoboda, K. Experience-dependent and cell-type-specific spine growth in the neocortex. *Nature* **441**, 979–983, <https://doi.org/10.1038/nature04783> (2006).
23. Majewska, A. K., Newton, J. R. & Sur, M. Remodeling of synaptic structure in sensory cortical areas *in vivo*. *J Neurosci* **26**, 3021–3029, <https://doi.org/10.1523/JNEUROSCI.4454-05.2006> (2006).
24. Grillo, F. W. *et al.* Increased axonal bouton dynamics in the aging mouse cortex. *Proc Natl Acad Sci USA* **110**, E1514–1523, <https://doi.org/10.1073/pnas.1218731110> (2013).
25. Cruz-Martín, A., Crespo, M. & Portera-Cailliau, C. Delayed stabilization of dendritic spines in fragile X mice. *J Neurosci* **30**, 7793–7803, <https://doi.org/10.1523/JNEUROSCI.0577-10.2010> (2010).
26. Murmu, R. P., Li, W., Holtmaat, A. & Li, J. Y. Dendritic spine instability leads to progressive neocortical spine loss in a mouse model of Huntington's disease. *J Neurosci* **33**, 12997–13009, <https://doi.org/10.1523/JNEUROSCI.5284-12.2013> (2013).
27. Jackson, J. S. *et al.* Altered Synapse Stability in the Early Stages of Tauopathy. *Cell Rep* **18**, 3063–3068, <https://doi.org/10.1016/j.celrep.2017.03.013> (2017).
28. Dong, H., Martin, M. V., Chambers, S. & Csernansky, J. G. Spatial relationship between synapse loss and beta-amyloid deposition in Tg2576 mice. *J Comp Neurol* **500**, 311–321, <https://doi.org/10.1002/cne.21176> (2007).
29. Walsh, D. M. & Selkoe, D. J. Deciphering the molecular basis of memory failure in Alzheimer's disease. *Neuron* **44**, 181–193, <https://doi.org/10.1016/j.neuron.2004.09.010> (2004).
30. Liebscher, S. *et al.* Chronic gamma-secretase inhibition reduces amyloid plaque-associated instability of pre- and postsynaptic structures. *Mol Psychiatry* **19**, 937–946, <https://doi.org/10.1038/mp.2013.122> (2014).
31. Burgold, S., Filszer, S., Dorostkar, M. M., Schmidt, B. & Herms, J. *In vivo* imaging reveals sigmoidal growth kinetic of beta-amyloid plaques. *Acta Neuropathol Commun* **2**, 30, <https://doi.org/10.1186/2051-5960-2-30> (2014).
32. Meyer-Lindemann, M. *et al.* Rapid appearance and local toxicity of amyloid-beta plaques in a mouse model of Alzheimer's disease. *Nature* **451**, 720–724, <https://doi.org/10.1038/nature06616> (2008).
33. Hefendehl, J. K. *et al.* Long-term *in vivo* imaging of beta-amyloid plaque appearance and growth in a mouse model of cerebral beta-amyloidosis. *J Neurosci* **31**, 624–629, <https://doi.org/10.1523/JNEUROSCI.5147-10.2011> (2011).
34. McCarter, J. F. *et al.* Clustering of plaques contributes to plaque growth in a mouse model of Alzheimer's disease. *Acta Neuropathol* **126**, 179–188, <https://doi.org/10.1007/s00401-013-1137-2> (2013).
35. Demattos, R. B. *et al.* A plaque-specific antibody clears existing beta-amyloid plaques in Alzheimer's disease mice. *Neuron* **76**, 908–920, <https://doi.org/10.1016/j.neuron.2012.10.029> (2012).
36. Yuan, P. *et al.* TREM2 Haplodeficiency in Mice and Humans Impairs the Microglia Barrier Function Leading to Decreased Amyloid Compaction and Severe Axonal Dystrophy. *Neuron* **90**, 724–739, <https://doi.org/10.1016/j.neuron.2016.05.003> (2016).
37. Condello, C., Schain, A. & Grutzendler, J. Multicolor time-stamp reveals the dynamics and toxicity of amyloid deposition. *Sci Rep* **1**, 19, <https://doi.org/10.1038/srep00019> (2011).
38. Condello, C., Yuan, P., Schain, A. & Grutzendler, J. Microglia constitute a barrier that prevents neurotoxic protofibrillar Abeta42 hotspots around plaques. *Nat Commun* **6**, 6176, <https://doi.org/10.1038/ncomms7176> (2015).
39. Mann, A. P. *et al.* Identification of a peptide recognizing cerebrovascular changes in mouse models of Alzheimer's disease. *Nature communications* **8**, 1403, <https://doi.org/10.1038/s41467-017-01096-0> (2017).
40. Thanopoulou, K., Fragkouli, A., Stylianopoulou, F. & Georgopoulos, S. Scavenger receptor class B type I (SR-BI) regulates perivascular macrophages and modifies amyloid pathology in an Alzheimer mouse model. *Proceedings of the National Academy of Sciences* **107**, 20816, <https://doi.org/10.1073/pnas.1005888107> (2010).
41. Banerjee, G. *et al.* The increasing impact of cerebral amyloid angiopathy: essential new insights for clinical practice. *Journal of neurology, neurosurgery, and psychiatry* **88**, 982–994, <https://doi.org/10.1136/jnnp-2016-314697> (2017).
42. Jiang, J., Wang, H., Li, W., Cao, X. & Li, C. Amyloid Plaques in Retina for Diagnosis in Alzheimer's Patients: a Meta-Analysis. *Front Aging Neurosci* **8**, 267, <https://doi.org/10.3389/fnagi.2016.00267> (2016).
43. Moolman, D. L., Vitolo, O. V., Vonsattel, J. P. & Shelanski, M. L. Dendrite and dendritic spine alterations in Alzheimer models. *J Neurocytol* **33**, 377–387, <https://doi.org/10.1023/B:NEUR.0000044197.83514.64> (2004).
44. Koffie, R. M. *et al.* Oligomeric amyloid beta associates with postsynaptic densities and correlates with excitatory synapse loss near senile plaques. *Proc Natl Acad Sci USA* **106**, 4012–4017, <https://doi.org/10.1073/pnas.0811698106> (2009).
45. Sze, C. I. *et al.* Loss of the presynaptic vesicle protein synaptophysin in hippocampus correlates with cognitive decline in Alzheimer disease. *J Neuropathol Exp Neurol* **56**, 933–944, <https://doi.org/10.1097/00005072-199708000-00011> (1997).
46. De Paola, V. *et al.* Cell type-specific structural plasticity of axonal branches and boutons in the adult neocortex. *Neuron* **49**, 861–875, <https://doi.org/10.1016/j.neuron.2006.02.017> (2006).
47. Yu, Y., Jans, D. C., Winblad, B., Tjernberg, L. O. & Schedin-Weiss, S. Neuronal A β 42 is enriched in small vesicles at the presynaptic side of synapses. *Life Science Alliance* **1**, <https://doi.org/10.26508/lsa.201800028> (2018).
48. Stephen, T. L. *et al.* APOE genotype and sex affect microglial interactions with plaques in Alzheimer's disease mice. *Acta Neuropathol Commun* **7**, 82, <https://doi.org/10.1186/s40478-019-0729-z> (2019).
49. Hoover, B. R. *et al.* Tau mislocalization to dendritic spines mediates synaptic dysfunction independently of neurodegeneration. *Neuron* **68**, 1067–1081, <https://doi.org/10.1016/j.neuron.2010.11.030> (2010).
50. Knowles, J. K. *et al.* The p75 neurotrophin receptor promotes amyloid-beta(1-42)-induced neuritic dystrophy *in vitro* and *in vivo*. *J Neurosci* **29**, 10627–10637, <https://doi.org/10.1523/JNEUROSCI.0620-09.2009> (2009).
51. McLeod, F. *et al.* Wnt Signaling Mediates LTP-Dependent Spine Plasticity and AMPAR Localization through Frizzled-7 Receptors. *Cell Rep* **23**, 1060–1071, <https://doi.org/10.1016/j.celrep.2018.03.119> (2018).
52. Kim, T. *et al.* Human LILRB2 is a beta-amyloid receptor and its murine homolog PirB regulates synaptic plasticity in an Alzheimer's model. *Science* **341**, 1399–1404, <https://doi.org/10.1126/science.1242077> (2013).
53. Zagrebelsky, M. *et al.* The p75 neurotrophin receptor negatively modulates dendrite complexity and spine density in hippocampal neurons. *J Neurosci* **25**, 9989–9999, <https://doi.org/10.1523/JNEUROSCI.2492-05.2005> (2005).
54. Brown, J. T., Chin, J., Leiser, S. C., Pangalos, M. N. & Randall, A. D. Altered intrinsic neuronal excitability and reduced Na⁺ currents in a mouse model of Alzheimer's disease. *Neurobiol Aging* **32**, 2109 e2101–2114, <https://doi.org/10.1016/j.neurobiolaging.2011.05.025> (2011).

Acknowledgements

This work was funded by Eli Lilly and Company and grants from the Medical Research Council and the Alzheimer's Society (to F.T. and A.R.).

Author Contributions

J.S.J., F.T., A.R., M.L.H. and M.J.O.N. designed the study, T.S. analysed the *in vivo* data; F.T., J.S.J. and T.S. carried out the *in vivo* experiments; J.P. carried out the CLARITY experiments; K.S., J.H., A.O.-E., T.K.M. and Z.A. characterized the model; A.R., M.J.O.N., J.S.J. jointly supervised the project.

Additional Information

Supplementary information accompanies this paper at <https://doi.org/10.1038/s41598-019-50781-1>.

Competing Interests: This work was conducted at Eli Lilly's research laboratories and several authors are/were employees of Eli Lilly.

Publisher's note Springer Nature remains neutral with regard to jurisdictional claims in published maps and institutional affiliations.



Open Access This article is licensed under a Creative Commons Attribution 4.0 International License, which permits use, sharing, adaptation, distribution and reproduction in any medium or format, as long as you give appropriate credit to the original author(s) and the source, provide a link to the Creative Commons license, and indicate if changes were made. The images or other third party material in this article are included in the article's Creative Commons license, unless indicated otherwise in a credit line to the material. If material is not included in the article's Creative Commons license and your intended use is not permitted by statutory regulation or exceeds the permitted use, you will need to obtain permission directly from the copyright holder. To view a copy of this license, visit <http://creativecommons.org/licenses/by/4.0/>.

© The Author(s) 2019